Generation of high resolution sea surface temperature using multi-satellite data for operational oceanography

YANG Chan-Su[1, 2, 3], KIM Sun-Hwa[1]*, OUCHI Kazuo[1], BACK Ji-Hun[1]

[1] Korea Ocean Satellite Center, Korea Institute of Ocean Science & Technology (KIOST), Ansan 426–744, Korea

[2] Ocean Science and Technology School, Korea Maritime and Ocean University, Busan 606–791, Korea

[3] Marine Environmental System Science, Korea University of Science and Technology, Daejeon 305–350, Korea

Abstract

In the present article, we introduce a high resolution sea surface temperature (SST) product generated daily by Korea Institute of Ocean Science and Technology (KIOST). The SST product is comprised of four sets of data including eight-hour and daily average SST data of 1 km resolution, and is based on the four infrared (IR) satellite SST data acquired by advanced very high resolution radiometer (AVHRR), Moderate Resolution Imaging Spectroradiometer (MODIS), Multifunctional Transport Satellites-2 (MTSAT-2) Imager and Meteorological Imager (MI), two microwave radiometer SSTs acquired by Advanced Microwave Scanning Radiometer 2 (AMSR2), and WindSAT with *in-situ* temperature data. These input satellite and *in-situ* SST data are merged by using the optimal interpolation (OI) algorithm. The root-mean-square-errors (RMSEs) of satellite and *in-situ* data are used as a weighting value in the OI algorithm. As a pilot product, four SST data sets were generated daily from January to December 2013. In the comparison between the SSTs measured by moored buoys and the daily mean KIOST SSTs, the estimated RMSE was 0.71°C and the bias value was –0.08°C. The largest RMSE and bias were 0.86 and –0.26°C respectively, observed at a buoy site in the boundary region of warm and cold waters with increased physical variability in the Sea of Japan/East Sea. Other site near the coasts shows a lower RMSE value of 0.60°C than those at the open waters. To investigate the spatial distributions of SST, the Group for High Resolution Sea Surface Temperature (GHRSST) product was used in the comparison of temperature gradients, and it was shown that the KIOST SST product represents well the water mass structures around the Korean Peninsula. The KIOST SST product generated from both satellite and buoy data is expected to make substantial contribution to the Korea Operational Oceanographic System (KOOS) as an input parameter for data assimilation.

Key words: SST, satellite, *in-situ*, high resolution, OI

1 Introduction

Numerical models for the operational ocean analysis and prediction system require high resolution SST products in real time or near-real time as input data (Guan and Kawamura, 2004; Donlon et al., 2007). Since the 1970s to date, various SST data have been provided by infrared radiometers and microwave radiometers onboard more than 10 satellites (Sakaida et al., 2009; Chao et al., 2009). Among them, polar-orbit satellites have provided infrared SST data four times per day with a high spatial resolution of 1 km such as those from AVHRR and MODIS (Guan and Kawamura, 2004; Goodrum et al., 2000; He et al., 2003). Similarly, SST data with high temporal resolution of 30 min to 1 h have been acquired by geostationary satellites including the Geostationary Operational Environmental Satellites (GOES) (Legeckis and Zhu, 1997; Wu et al., 1999). These infrared (IR) SST data are severely limited by the presence of clouds and high concentrations of aerosols. Although microwave radiometers can acquire SST under cloud cover, the spatial resolution of about 25–50 km

is much lower than IR data (Guan and Kawamura, 2004). For generating the cloud-free, high spatial and temporal resolution SST, there have been many attempts to combine various IR and microwave SST data (Guan and Kawamura, 2004; Sakaida et al., 2009; Chao et al., 2009). Recently, an international collaboration of operational and research agencies is producing a new generation of SSTs, combining satellite microwave and IR data, and *in-situ* observations for the numerical weather prediction (NWP), ocean forecasting, ecosystem applications, and climate research (Donlon et al., 2007). To improve the SST observation capability, the Global Ocean Data Assimilation Experiment (GODAE) conducted the Group for High-Resolution SST Pilot Project (GHRSST-PP) (Donlon et al., 2004). The GHRSST-PP enhanced and reformatted the existing SST data to generate scientifically and technically feasible new SST products of high quality (Donlon et al., 2007) by merging SST data from the multiple satellites and *in-situ* observation (Reynolds, 1988; Reynolds and Smith, 1994; Reynolds et al., 2005; Chao et al., 2009). However, there are

* Corresponding author, E-mail: scorpio96@kiost.ac.kr

some issues to be considered in the merging process. For example, the differences between the skin/subskin and bulk SSTs need to be taken into consideration (Chao et al., 2009), and the bias correction between the satellite and *in-situ* data is required (Chao et al., 2009; Martin et al., 2012; Donlon et al., 2012). The SST merging algorithms also have the diurnal variations which are important to produce high-quality daily SST products (Tanahashi et al., 2000; Kawai et al., 2006; Wick et al., 2002). Another issue to be considered is the geometric matching of satellite and *in-situ* data.

Since 2009, the KIOST has been developing the Korea Operational Oceanographic System (KOOS) which provides nowcasts and forecasts of ocean information around the Korea Peninsula to support marine activities and to mitigate coastal disasters (Lee et al., 2009). As an important subsystem of the KOOS, the KIOST SST production and service system has been developed. The KIOST SST is the first system of its kind providing high spatial and temporal SST data generated by merging multi-satellite SSTs in Korea. The SST of single satellite sensor as AVHRR and MI is only serviced from Korea public institutions related on ocean and meteorology (National Institute of Meteorological Research, 2013; Park et al., 2014). This paper analyzes the differences among various satellite SST data and *in-situ* data, and introduces the KIOST SST system to generate and provide the high spatial and temporal resolution SST product by merging six satellites including Advanced Very High Resolution Radiometer (AVHRR), Moderate Resolution Imaging Spectroradiometer (MODIS), Multi-functional Transport Satellite-2 (MTSAT-2) Imager, Meteorological Imager (MI), WindSAT, Advanced Microwave Scanning Radiometer 2 (AMSR2) and *in-situ* SSTs. Although the merging algorithm of KIOST SST is based on the New Generation Sea

Surface Temperature (NGSST) optimal interpolation (OI) algorithm, the OI algorithm of the KIOST SST system considers the Root-Mean-Square-Error (RMSE) between satellites and *in-situ* SSTs as a weighting parameter of the merging algorithm to improve the accuracy of merging SST data. To reduce the diurnal variation, the KIOST SST product is produced every 8 h in the waters around the Korean peninsula. The KIOST SST provides higher spatial resolution of 1 km and temporal resolution of 8 h than other GHRSSTs.

In the following, the datasets used in this study are described in Section 2. The SST merging algorithm is described in detail in Section 3, and Section 4 presents the evaluation results of spatial quality and quantitative accuracy of the KIOST SST product. The conclusions are presented and further studies are suggested in Section 5.

## 2 Datasets

2.1 *Satellite data*

This study used a total of six satellite SST data having various spatial and temporal resolutions as shown in Table 1. High spatial resolution (1 km) SSTs by the polar-orbiting satellites include the MODIS SSTs onboard Terra and Aqua, and AVHRR SSTs onboard NOAA-16, 18 and 19. MODIS and AVHRR SSTs data are generated directly in real-time twice a day using the TeraScan software in the Korea Ocean Satellite Center (KOSC) in KIOST. MI is an intermediate resolution (4 km) IR sensor onboard COMS (Communication, Ocean and Meteorological Satellite) which is a new geostationary satellite of Korea, launched in July 2010. Geostationary satellite SSTs of resolution 5 km are provided with high temporal resolution. The MI and MTSAT-2 SSTs are generated

Table 1. Specifications of the satellite data

Sensor/satellite	Spatial resolution	Temporal resolution (LT)	Sensor type	Orbit
MODIS/Terra, Aqua	1 km	twice per day (Aqua: 01:00–03:00, Terra: 10:00–12:00 am, pm)	infrared	polar
AVHRR/NOAA-16, 18, 19	1 km	twice per day (NOAA-16: 09:00–12:00, NOAA-18: 04:00–07:00, NOAA-19: 00:00–03:00 am, pm)	infrared	polar
MI/COMS	4 km	15 min	infrared	geostationary
MTSAT-2 Imager/MTSAT-2	5 km	1 h	infrared	geostationary
AMSR2/GCOM-W1	50 km	twice per day (00:00–04:00, 14:00–18:00)	microwave	polar
WindSAT	25 km	twice per day (00:00–06:00, 18:00–24:00)	microwave	polar

every 15 min and 1 h respectively. Although many IR SST data were acquired for the present study, those with large cloud cover were not used for the fusion with *in-situ* data. If no IR SST data were available, SSTs measured by microwave radiometers onboard WindSAT and AMSR2 were used for the fusion despite their low spatial resolution (25–50 km as in Table 1). WindSAT is a spaceborne polarimetric microwave radiometer developed by the Naval Research Laboratory and supported by the NASA's Earth Science Enterprise Program. AMSR2 is onboard the GCOM-W1 satellite developed by Japan Aerospace Exploration Agency (JAXA).

The coverage of each satellite SST product received by the KIOST SST system and study areas are shown in Fig. 1. Because the KIOST SST uses global WindSAT and AMSR2 SST products, the coverage of two microwave SST data are not included in Fig. 1. For rapid processing of large amount of SST data and for the users' interest, the KIOST SST product covers only the local area
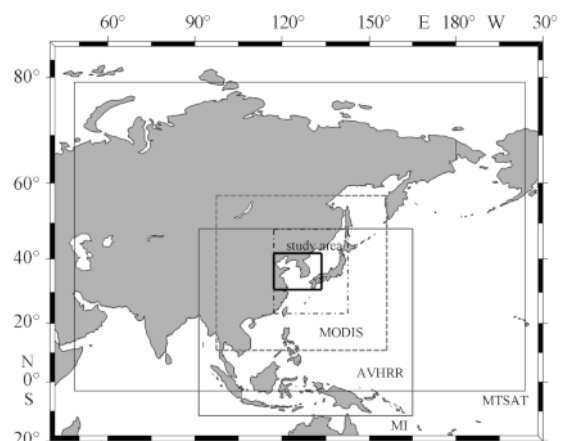
Fig. 1. Coverage of multiple satellite SST products and KIOST SST product.

(longitude: 117.25°–133.73°E, latitude: 32.51°–41.48°N) centered at the Korean Peninsula.

2.2 *In-situ data*

In producing different satellite SST products, it is desirable to evaluate the accuracy of SST data using the *in-situ* temperature data (May et al., 1998). In this study, the *in-situ* data measured by eight moored buoys are used not only to calculate the RMSE values, but also to blend with satellite data. The ID, name, locations, and floating radii of these buoys are shown in Table 2. Temperature is measured at 1 m depth. Because the Donghae and Ulleung buoys had the floating radii over 1 km, it is necessary to make the geometric matching of satellite and *in-situ* SST data.

Figure 2 shows the distribution of the eight moored buoys of

Table 2. IDs and positions of eight buoys for *in-situ* data measurements.

Buoy ID	Buoy name	Latitude (N)	Longitude (E)	Floating radius/m	Distance from coast or island/km
22101	Deokjeok	37.23°	126.02°	69	3.95
22103	Geomun	34.00°	127.50°	127	10.35
22104	Geoje	34.77°	128.90°	124	14.74
22105	Donghae	37.53°	130.00°	1 192	68.13
22106	Pohang	36.35°	129.78°	326	32.47
22107	Mara	33.08°	126.03°	152	22.41
22108	Oeyeon	36.25°	125.75°	89	18.39
21229	Ulleung	37.23°	131.65°	1 755	18.92

IDs listed in Table 2. The Deokjeok buoy (ID 22101) has the smallest floating radius of 69 m at distance approximately 4 km away from the nearest island, while the Ulleung buoy (ID 21229) has the largest floating radius of 1.8 km and is located at 19 km distance away from the nearest island. The two buoys (ID 22101, 22108) in the Yellow Sea have small floating radii of less than 100 m and are located near the coastal area. The buoys (ID 21229, 22105, 22106) in the Sea of Japan/East Sea are located in the open water. The Donghae buoy (ID 22105) is at the farthest from the east coast by the distance 68 km, and the floating radius is second largest (1.2 km). Three buoys (ID 22103, 22104, 22107) in the Southern Sea are located at the positions along the line of Busan and Jeju Island.

Fig. 2. Locations and distributions of the Korea Meteorological Administration (KMA) moored buoys as listed in Table 2 in the KIOST SST coverage.

2.3 *In-situ data*

The validation of the KIOST SST product is made using the GHRSST level 4 data for their high spatial (1 km) and temporal (daily) resolutions as well as their high data quality. This is because the type of KIOST SST data is different from other types and also there is a severe problem in geometric registration. The GHRSST product is produced daily by JPL OurOcean group using a multi-scale two-dimensional variation (MS-2DVAR) merging algorithm which is capable of merging eight satellite (AVHRR, AATSR, SEVIRI, AMSRE, TMI, MODIS, GOES, and MT-SAT-1R) SST data. This computationally efficient algorithm has also a RMSE of less than 1°C as compared with the *in-situ* data (Chao et al., 2009).

3 Methods

3.1 *Reception of satellite and in-situ data*

The KIOST SST system is composed of three steps as illustrated in Fig. 3. The first step is the reception of satellite and *in-situ* SST data, where the real-time MODIS and AVHRR data are received through the KIOST KOSC server. The MI, MTSAT-2, WindSAT, and the *in-situ* buoy data are received through the FTP server of Korea Meteorological Administration (KMA), while AMSR2 SST data are provided through the JAXA FTP server. Each *in-situ* buoy measures the surface temperature continuously in real-time, and the information is provided by the KMA. The second step is pre-processing of the received data such as removal of cloud areas and resampling for quality control. In the third step, the six satellites and *in-situ* SST data are blended by using the OI algorithm. The latter two steps are described further in detail in the following subsections.

3.2 *Pre-processing*

The aim of the pre-processing is to remove the pixels corresponding to cloud areas and also resample the satellite and *in-situ* data with a same spatial and temporal resolution scale. First, all those data are classified into three SST datasets at 8 h intervals (LT 00:00–08:00, 08:00–16:00, 16:00–24:00). Then, the maximum SST composite method is applied to each satellite SST dataset to remove the pixels of low SST values due to cloud and aerosol. The maximum SST value is compared with a mean SST product according to the following criterion.

$$SST_i - \overline{SST} \leqslant -3°\text{C}, \tag{1}$$
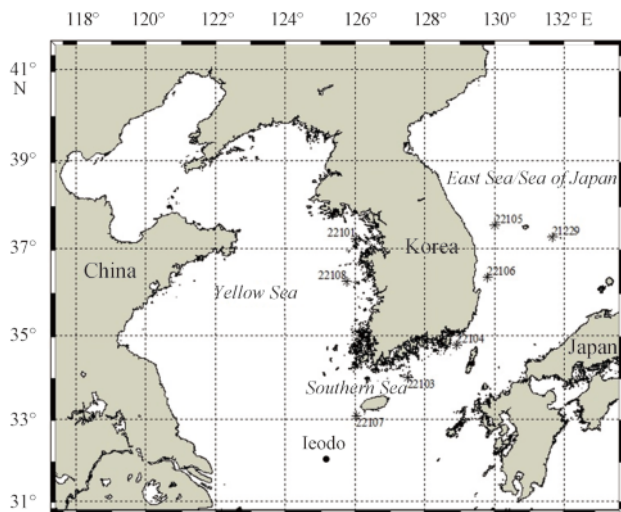
where $\overline{SST}$ means the daily mean SST value of the previous day and SST_i is the i-th SST value. The threshold value of –3°C was empirically determined, which is close to the standard deviation of SST variations in the study region. Before merging SSTs, all satellite SST images are resampled at an interval of 1 km spatial resolution using a cubic convolution algorithm and land areas are masked out.
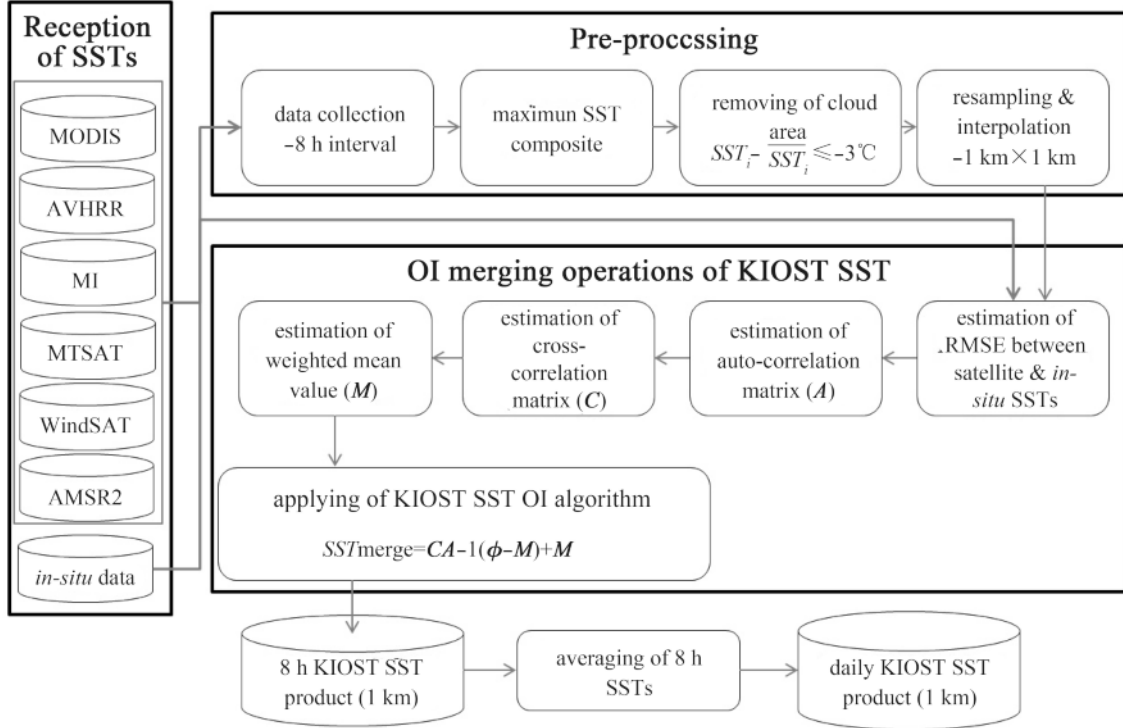

Fig. 3. Illustrating three processing steps of KIOST SST products.

3.3 *KIOST SST optimal interpolation method for merging SSTs*

The optimal interpolation (OI) algorithm based on the Gauss-Markoff theorem was introduced into oceanic data analyses by Bretherton et al. (1976). Because the OI algorithm is easy to implement, it has also been applied to satellite SSTs data and is still most commonly used for merging SSTs (Guan and Kawamura, 2004; Chao et al., 2009). The KIOST SST algorithm developed based on the NGSST-O system generates SSTs products with improved spatial and temporal resolutions.

The OI algorithm of KIOST SST product is based on the following equation (Guan and Kawamura, 2004).

$$SST_{\mathrm{merge}} = CA^{-1}(\phi - M) + M, \tag{2}$$

where SST_{merge} is the estimated SST, ϕ is the matrix of top 150 SSTs in a priority list calculated from the input SST data, A^{-1} is the inverse of the autocorrelation matrix of satellite SSTs, M is the weighted mean scalar estimated by using RMSE of input satellite SSTs, and C is the cross-correlation matrix between the estimated and satellite SSTs, which is given by (Carter and Robinson, 1987)

$$C(\gamma_i) = (1 - \gamma_i^2)\exp(-\gamma_i^2/2). \tag{3}$$

The square of cross-correlation coefficient γ_i^2 is defined by the following equation.

$$\gamma_i^2 = \left(\frac{\Delta x_i}{L}\right)^2 + \left(\frac{\Delta y_i}{L}\right)^2 + \left(\frac{\Delta t_i}{D}\right)^2. \tag{4}$$

The square of cross-correlation coefficient γ_i^2 is defined by the following equation, where Δx_i and Δy_i are respectively the zonal and meridional distances between the estimation and observation points, i.e., the zonal axis is orthogonal to the meridional ax-

is, Δt_i is the temporal difference between the estimation and observation times, L is the spatial decorrelation scale (L=0.5°), and D is the temporal decorrelation scale (D=2 d). Guan and Kawamura (2004) and Sakaida et al. (2009) suggested L =1°, but we adopted empirically L=0.5° because the study area has a large spatial variability.

Using selected SST data, the autocorrelation matrix is given by (Sakaida et al., 2009)

$$A = \varepsilon^2 + \exp(-\gamma^2), \tag{5}$$

where ε is the RMSE matrix for each satellite SST data. The RMSEs of the each satellite and *in-situ* SSTs obtained during 5 d are calculated by

$$\mathrm{RMSE} = \sqrt{\frac{1}{N}\sum_{i=1}^{N}(B_i - S_i)^2}. \tag{6}$$

In Eq. (6), B_i and S_i are the i-th *in-situ* and satellite SSTs, and N is the number of total *in-situ* data obtained within ± 2 d.

The weighted mean SST M is given by

$$M = \sum_i^{150} \omega_i SST_i, \tag{7}$$

$$\omega_i = 1/(\varepsilon_i^2 \times \sum_{i=1}^{150}\frac{1}{\varepsilon_1^2}), \tag{8}$$

where ε_i is the i-th RMSE between satellite and *in-situ* SSTs, and SST_i is the i-th satellite or *in-situ* SSTs. Note that ε_i is different from in Eq. (5). For computational efficiency in calculating M, the total of 150 SST data are selected with the highest weighted

values (ω_i). The weighted mean is used in the OI algorithm of KIOST SST product as in Eq. (2).

If the inverse of the autocorrelation matrix is invalid, the merged SST is given by M instead of Eq. (2) as by Guan and Kawamura (2004), i.e.,

$$SST_{\mathrm{merge}} = M. \tag{9}$$

The autocorrelation matrix (A) does not have an inverse matrix if the columns of A are linearly dependent on each other, or det (A) = 0.

Figure 4 shows the entire flow chart of producing KIOST SST every 8 h where daily KIOST SST product is generated by averaging three SSTs acquired every 8 h.
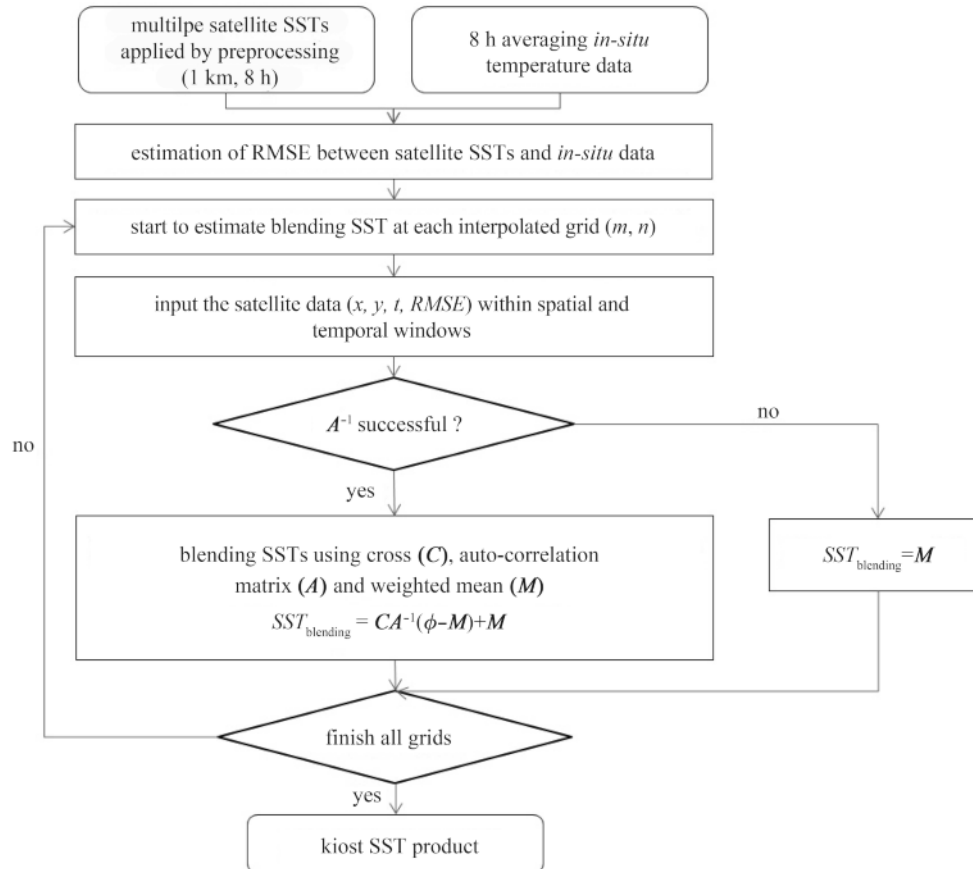

Fig. 4. Processing flow chart for KIOST SST OI algorithm.

4 Evaluation

4.1 *Cross-comparisons of input SST data*

The SSTs from the total of six satellites used in the KIOST SST system were compared with each other for estimating bias values for input data. Table 3 shows the acquisition times of the satellite data used for cross-comparison. Using satellite SSTs acquired at similar times on January 14, 2013, the cross-correlation analysis of input SSTs data was conducted. Note that there is substantial difference in the data acquisition times of WindSAT from other satellites, which needs to be taken into consideration for the analyses.

Figure 5 shows the various satellite SSTs of January 14, 2013. Compared with microwave SST data, IR SST data show heavy cloud covered areas, in particular, in the Japan/East Sea. Among IR SST data, MTSAT-2 shows higher SST than other IR SSTs. Due to the influence of the land on microwave emission, it is difficult to obtain SST information in the coastal waters (Guan and Kawamura, 2003). Nevertheless, in the waters well off the coasts, the patterns of microwave SST were found to be similar to those of IR SSTs.

All combinations of input satellite SSTs show strong correla-

tion with mean correlation coefficient (r) over 0.98. As to the SST values, the AVHRR SSTs are lower than the other IR SSTs as can be seen in Figs 6a, b and c, while the MTSAT-2 shows higher SSTs than those of other polar orbiting satellites. The microwave SSTs (WindSat and AMSR2) are higher than IR SSTs as in Figs 6d and e.

Table 3. Satellite SST data acquisition times used for comparing different satellite SSTs

Satellite	Acquisition time
AVHRR	2013.01.14 UTC 04:34
MODIS	2013.01.14 UTC 04:32
MI	2013.01.14 UTC 04:30
MTSAT-2	2013.01.14 UTC 04:33
AMSR2	2013.01.14 UTC 03:55
WindSAT	2013.01.14 UTC 09:03

With the results of cross-correlation between different satellite SSTs, the RMSE and bias of each satellite SST product were estimated by using *in-situ* SST data at eight buoy locations from January to May 2013 as shown in Fig. 7 and Table 4. Because the
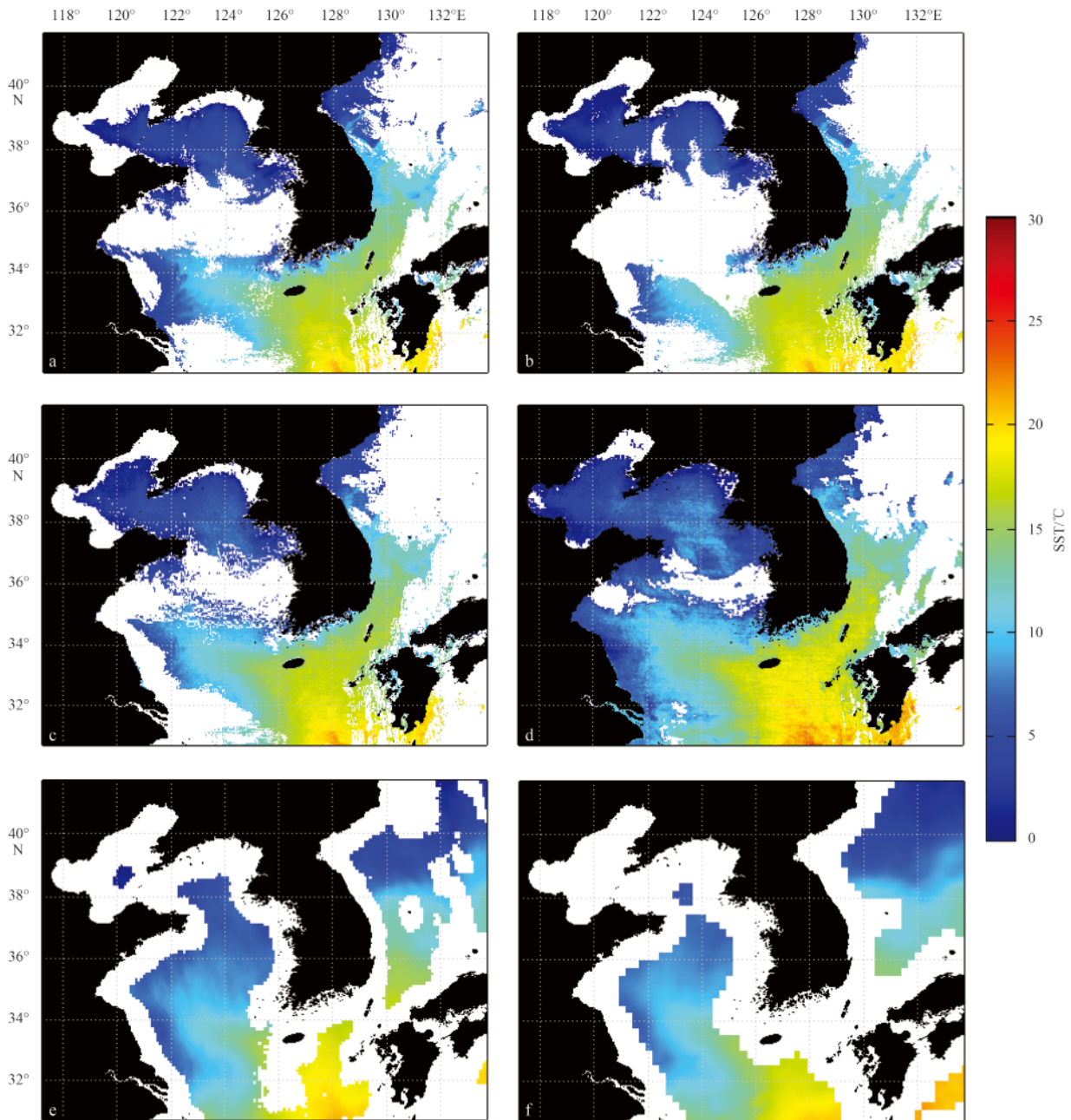
Fig. 5. AVHRR (a), MODIS (b), MI (c), MTSAT-2 (d), AMSR2 (e) and WindSAT (f) SSTs on January 14, 2013.

WindSAT and AMSR2 SSTs covered only the Ulleung site, these data were excluded from the comparison with *in-situ* data. As can be seen in Figs 7a–c, AVHRR tends to underestimate the *in-situ* data, and MODIS and MI SSTs appear to be in agreement with the *in-situ* SSTs. Overestimation of SSTs by MTSAT-2 is evident as in Fig. 7d. The reason for these differences is not certain, but may be associated with spatial resolution, i.e., the estimated SSTs tend to shift from underestimation to overestimation (AVHRR to MTSAT-2) with decreasing spatial resolution (1 km to 5 km) (also see Table 1). MTSAT-2 data have the largest mean bias SST with 1.29°C due to highest SST values as in Fig. 6c, followed by AVHRR with –0.67°C. The mean bias SSTs of MODIS and MI are 0.49°C and 0.11°C respectively (see Table 4). The AVHRR has smaller RMSE values than the MODIS SST data, while the MTSAT-2 SSTs show the largest RMSE value of 1.72°C. Although the accuracy of

microwave SST data is not estimated in this study, RMSEs of AM-SR2 and WindSat SST products are reported to be lower than 0.6°C in the preview validation studies (Shibata, 2013; Yili et al., 2014). These differences may be associated with bulk, subskin and skin SSTs. As to the RMSE and bias SSTs at different *in-situ* data acquisition positions shown in Table 4, the MI SSTs measured at all locations, except Geomun, have smallest RMSEs, and the MTSAT-2 SSTs have largest RMSEs above 1.0°C except Oeyeon and Ulleung. The RMSEs tend to be rather large in all satellite SSTs at the Geomun site among eight locations. The reason is not known, but it may be due to the geometric and temporal matching errors of satellite and *in-situ* data. Spatial and temporal SST variances are also large at this site where the Tsushima Warm Current flows.
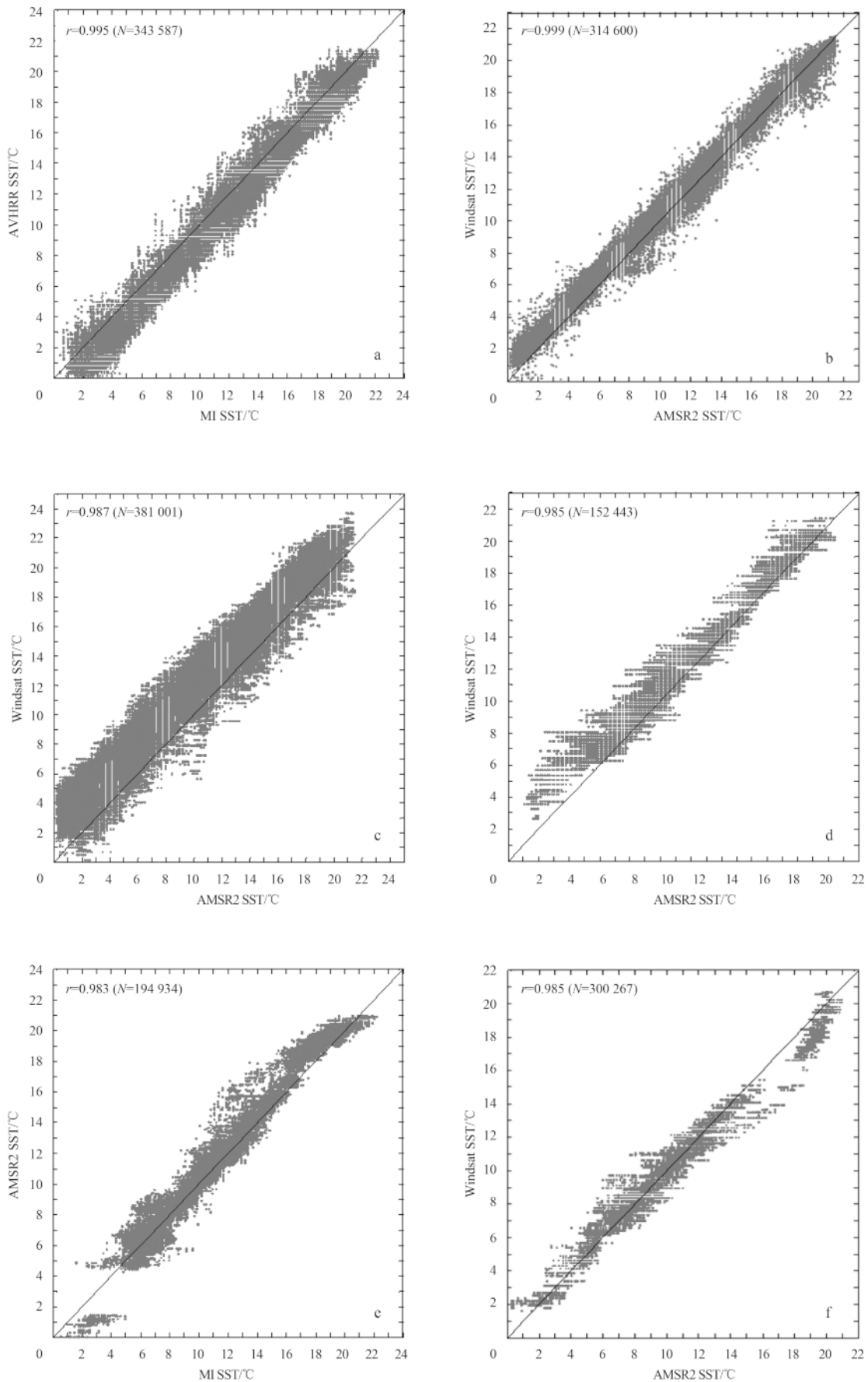
Fig. 6. The scatter diagrams of satellite SST data on January 14, 2013.

Table 4. Accuracy statistics of satellite SST data (°C) at eight sites

Satellite	RMSE				Bias (Satellite SST – *in-situ* SST)			
	AVHRR	MODIS	MI	MTSAT-2	AVHRR	MODIS	MI	MTSAT-2
Deokjeok	0.31	1.29	0.68	1.82	−0.14	0.34	0.28	1.27
Geomun	1.37	0.96	1.46	1.94	−0.38	0.24	1.20	2.57
Geoje	1.06	1.84	0.59	1.80	−0.83	1.23	−0.17	1.72
Donghae	0.80	1.40	0.55	1.67	−0.54	0.31	0.16	1.21
Pohang	0.88	1.13	0.57	2.23	−0.67	−0.83	0.17	2.18
Mara	1.60	1.77	0.42	1.46	−1.41	1.04	−0.15	0.87
Oeyeon	1.09	–	0.47	1.26	−0.84	1.43	−0.25	0.19
Ulleung	–	0.92	0.66	1.04	−0.55	0.14	−0.40	0.30
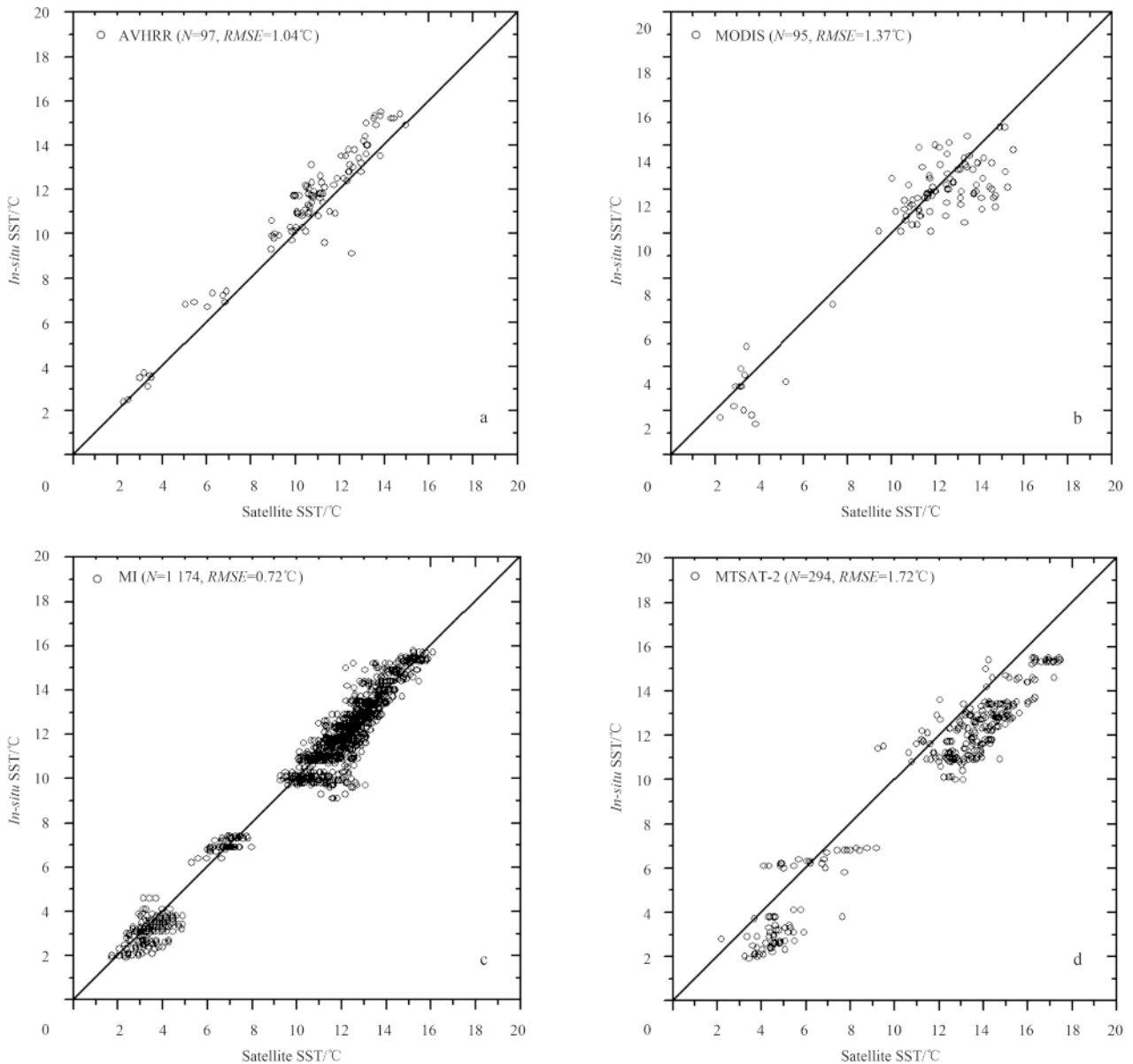
Fig. 7. The scatter diagram of IR SSTs and *in-situ* data from January to May 2013 for AVHRR (a), MODIS (b), MI (c), and MTSAT-2 (d).

4.2 *Evaluation of KIOST SST products*

The KIOST SST system generated 8 hourly and daily merging SSTs data from January to May 2013. Figure 8 shows the 8 hourly KIOST SST products of March 30, 2013, where, by close inspection, temporal changes can be seen in the central Yellow Sea and

parts of the Sea of Japan/East Sea. In the Fig. 8, SSTs are lowest along the coastal waters of the Yellow Sea and the northern coast of the Sea of Japan/East Sea, and rather complex patterns of SSTs including large eddies can be seen in the Sea of Japan/East Sea where warm currents of SST over 17°C from the Southern Sea

meet cold waters in the northern Sea of Japan/East Sea.

For objective evaluation of the KIOST SST data, daily KIOST SST and daily GHRSST level 4 data on March 30, 2013 were compared as shown in Fig. 9. The results show that the KIOST SST is higher by approximately 1°C than GHRSST in the high latitude areas of the Sea of Japan/East Sea as in Fig. 9g, but, on average, KIOST SST is slightly lower than the GHRSST. The difference may be caused by the different merging algorithms and different datasets used for the SST products. Figures 9c and d and Figs 9e and f are the enlarged areas of the upper yellow and lower white boxes in Figs 9a and b respectively. The temperature patterns observed

in the Sea of Japan/East Sea are generated by the interactions of the East Korea Warm Current (EKWC) off the east coast of Korea, the Liman Cold Current, and the North Korea Cold Current (NK-CC). The EKWC flows to north along the southeastern coast of the Korean peninsula, encounters the NKCC at around 38°N latitude, and veering to southeast, creating large eddies (Lee and Niiler, 2005). These coastal warm streamer of the EKWC and eddies are well matched to the KIOST SST as can be seen in the lower central area in Fig. 9c. These patterns will be discussed further with reference to the chlorophyll *a* distribution in Fig. 11.

The center-east region of the lower white boxes in Figs 9a
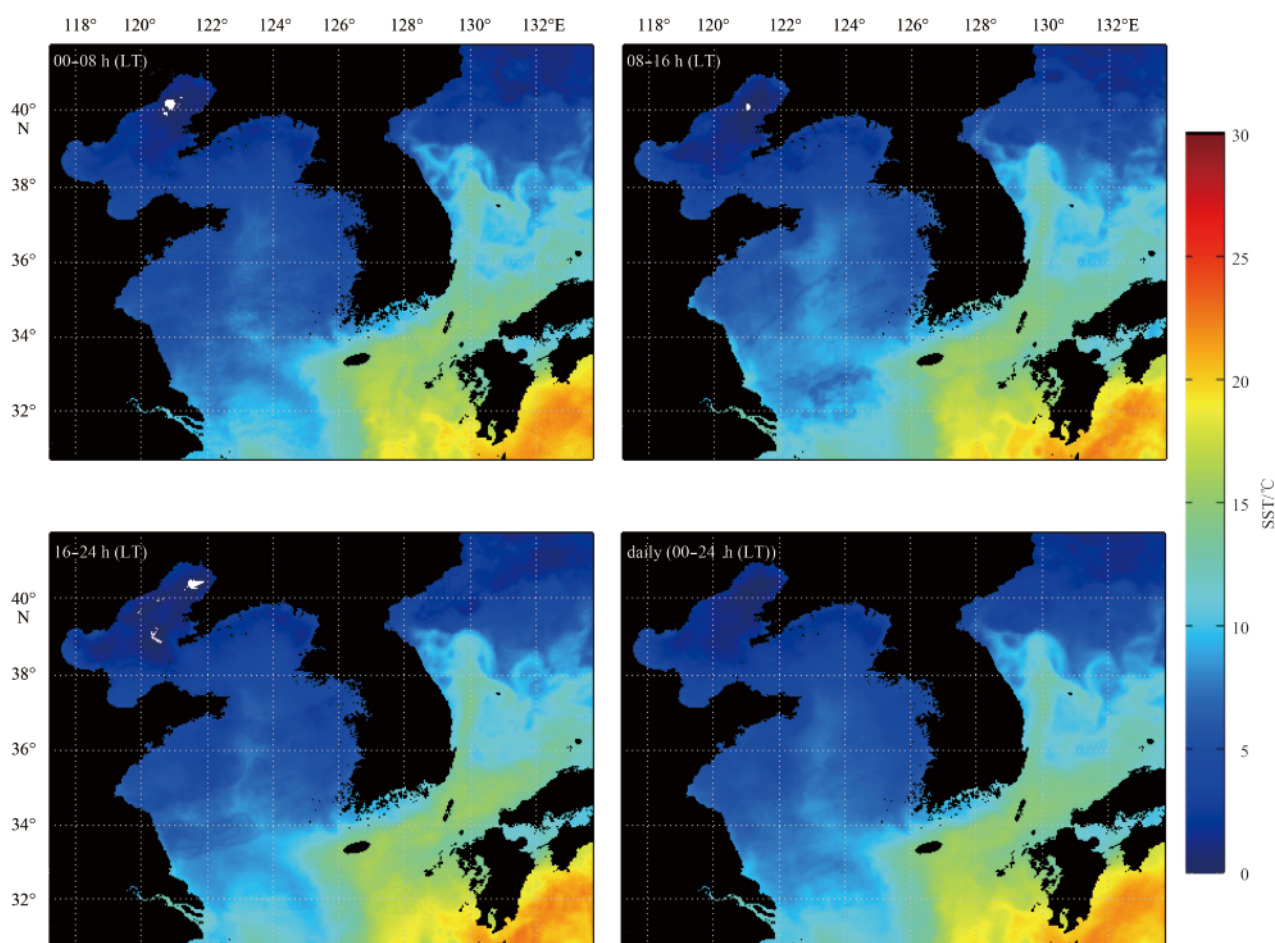
Fig. 8. Three 8 hourly and a daily average KIOST SSTs of March 30, 2013.

and b lies on the path of the Tsushima Warm Current, and the west area is the boundary between the Yellow Sea and Cheju Warm Current (Lie et al., 1998). The smooth and continuous flowing pattern of the Tsushima Warm Current can be seen in the KIOST SST in Fig. 9e. As can be seen in Fig. 9h, the KIOST SST and GHRSST are well correlated with the correlation coefficient of 0.99. From comparison with *in-situ* data, the accuracy was found to be less than 1°C for both the KIOST SST and GHRSST. However, the KIOST SST product has higher temporal resolution of 8 h than 24 h of the GHRSST product.

In order to evaluate the spatial variation of the KIOST SST data in detail, the horizontal SST gradients were calculated. Figure 10 shows the grid-point averaged east-west and north-south gradients of KIOST SST and GHRSST on March 30, 2013. Large

SST variations can be observed in the Sea of Japan/East Sea where warm and cold currents meet, and large variations are also seen in the Southern Sea where the strong Tsushima Warm Current flows. In the KSST SST, fine gradient structures can be seen, while they appear rather blurred in the GHRSST. The EKWC veering to southeast with large eddies in the Sea of Japan/East Sea is evident in Fig. 10c. A continuous flow pattern of the Tsushima Warm Current is also enhanced in Fig. 10e.

Figure 11 shows the chlorophyll a images extracted from Geostationary Ocean Color Imager (GOCI) data obtained on March 28 and 30, 2013 respectively, corresponding to the upper yellow and lower white boxes shown in Fig. 10. Slightly high chlorophyll *a* bands in the two circles in Fig. 11a are closely connected to the boundary between EKWC and NKCC, and match well to the KIOST
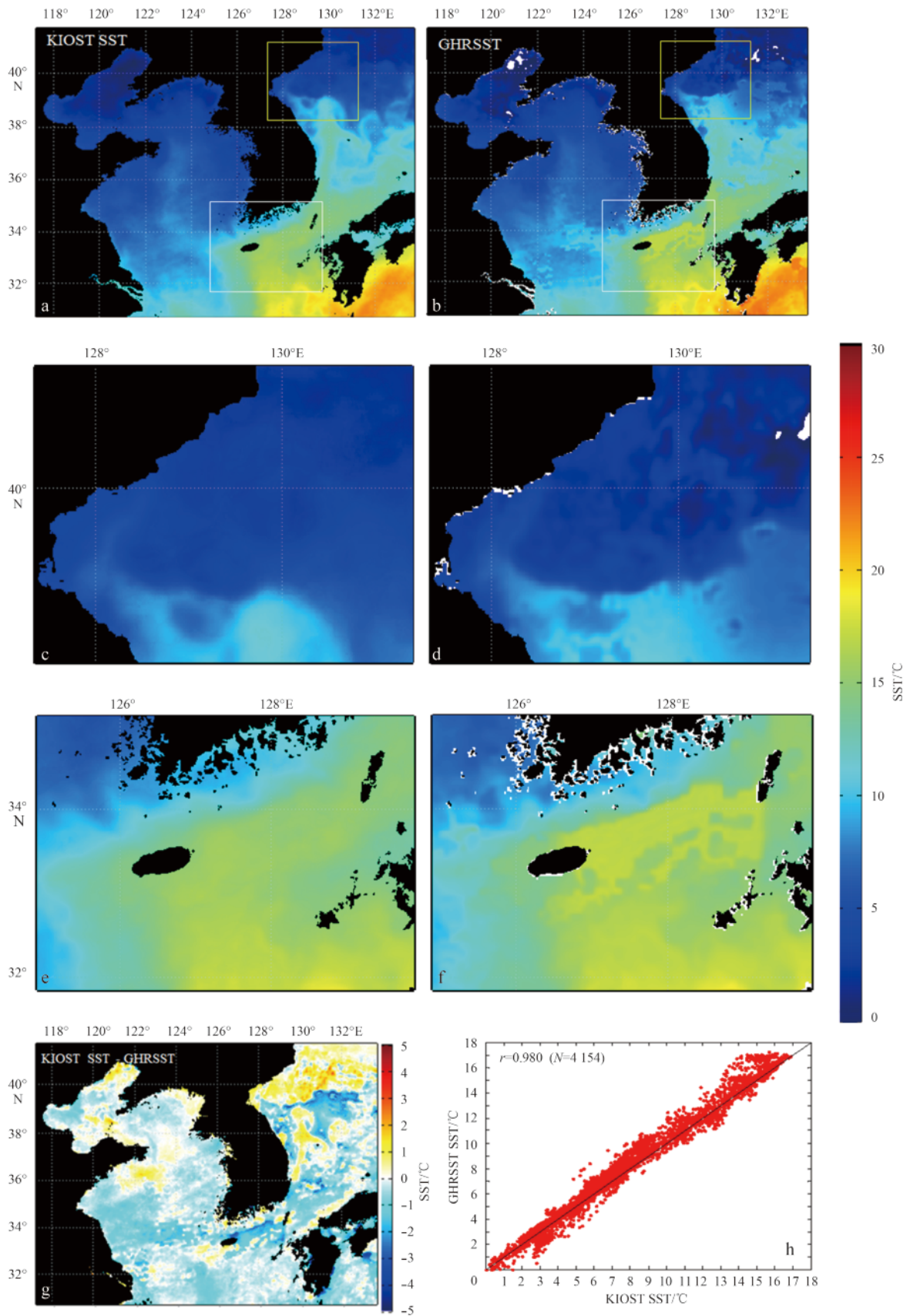
Fig. 9. Comparison of daily KIOST SST (a) and GHRSST (b), enlarged areas of the upper yellow box (c, d), and enlarged areas of the lower white box (e, f), difference between KIOST SST and GHRSST (g), and scatter diagram of KIOST SST and GHRSST (h) on March 30, 2013.

SST in Fig. 9c and temperature gradient in Fig. 10c. Low chlorophyll *a* regions (dotted ellipse) in the Fig. 11b correspond to the Tsushima Warm Current. This image does not match to such temperature variations as seen in the GHRSST shown in Figs 9f and 10f, but rather fits well to the KIOST SST patterns in Figs 9e and 10e. Thus, it can be said that the KIOST SST product represents well the water mass structures around the Korean Peninsula.

The KIOST SST products were compared with the total of 2 559 *in-situ* SSTs acquired by the eight moored buoys from January to December 2013. The range of KIOST and *in-situ* SST data is from 1 to 30°C as in Fig. 12. Two sites with SST values less than 10°C are located in the Yellow Sea except summer season, and
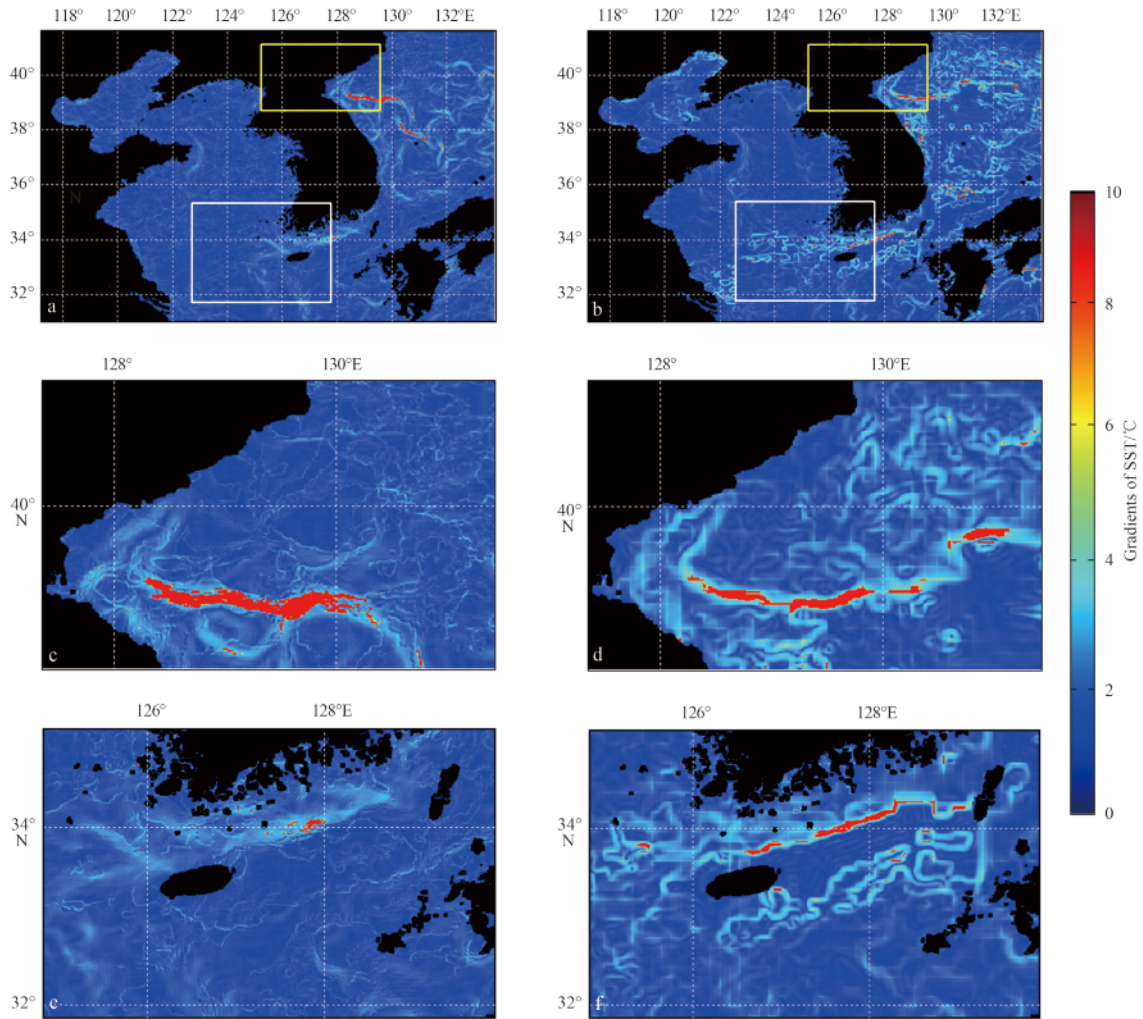
Fig. 10. Averaged east-west, north-south gradients of KIOST SST (left) and GHRSST (right) on March 30, 2013 for total study area (a and b), enlarged areas of the upper yellow boxes (c and d), and enlarged areas of the lower white boxes (e and f).
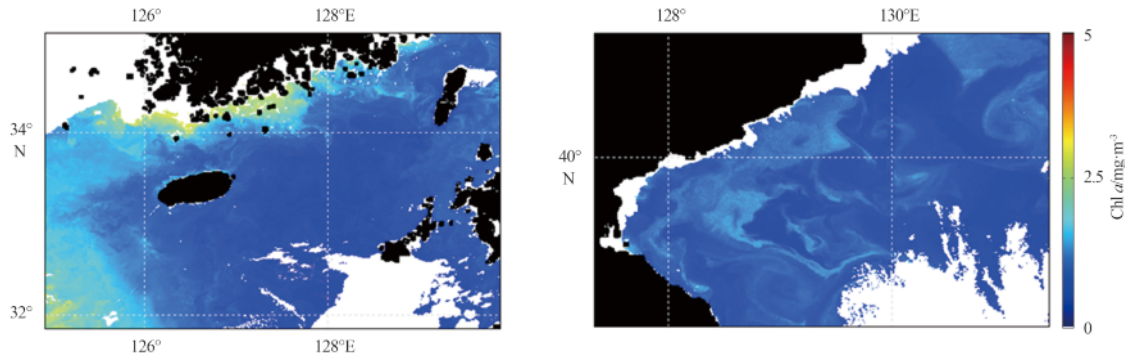
Fig. 11. Chlorophyll *a* images extracted from Geostationary Ocean Color Imager (GOCI) data obtained on March 31 (upper) and March 28, 2013 (lower), corresponding to the yellow and white boxes shown in Fig. 10. White color indicates the areas of cloud cover and noise.

the highest SST values are at the Mara site located in the southernmost area. As seen in Fig. 12, all KIOST SST products show strong correlation with *in-situ* data with mean correlation coefficient over 0.99. As seen in Fig. 12, the RMSE values of four KIOST SST products are less than 0.9°C and the KIOST SSTs are approximately 0.2°C lower than *in-situ* data. The accuracy of the daily averaged KIOST SST data is the highest among four KIOST SST products.

Table 5 shows the accuracy statistics of averaged daily KIOST SSTs from January to December 2013. On average, SSTs in the Southern Sea (Geoje and Mara sites) are highest, followed by those in the Sea of Japan/East Sea (Donghae, Pohang, and Ulleung sites) as expected, and SSTs in the Yellow Sea (at Deokjeok and Oeyeon sites) are lowest. At all eight sites, the RMSEs of the KIOST SSTs are less than 0.9°C with bias values within ±0.4°C.

Figure 13 shows the temporal variations of the RMSE of one-month average KIOST SSTs at eight sites from January to December 2013. The six sites except Geomun and Ulleung sites show higher RMSE values during spring (from March to May) and
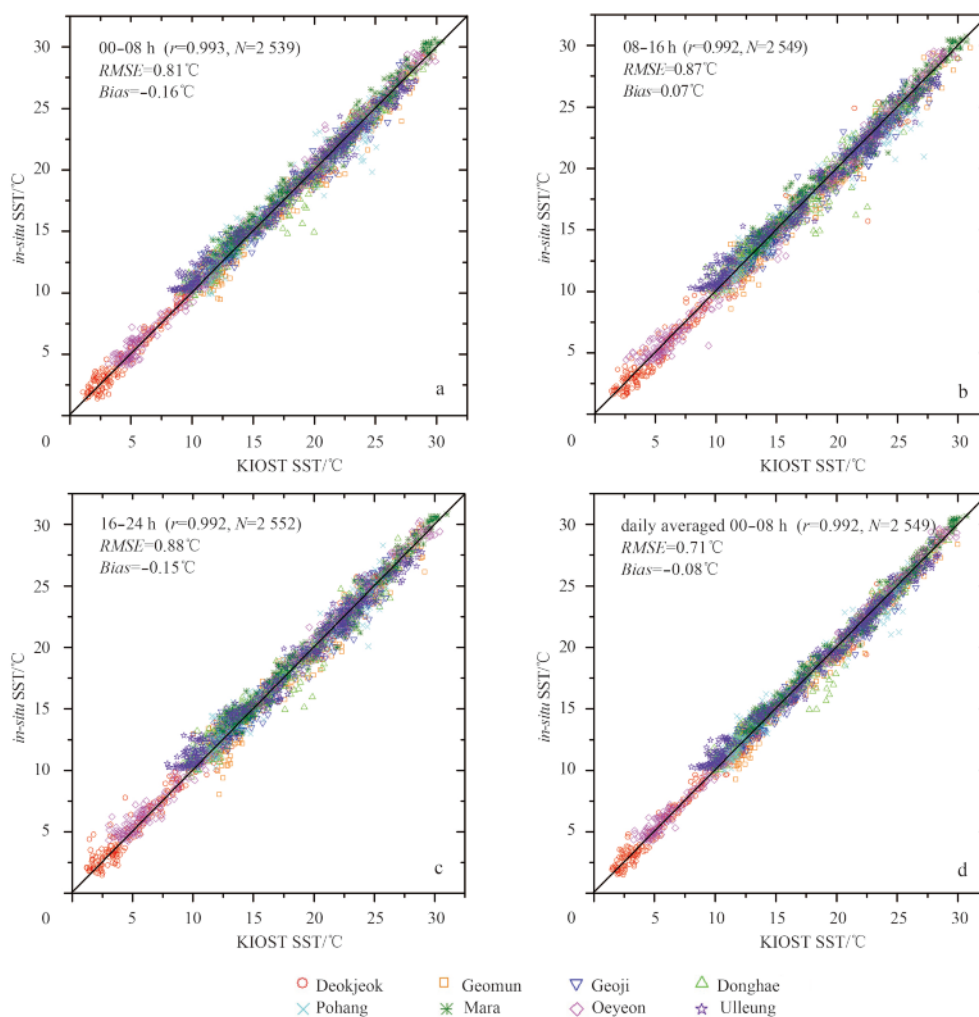
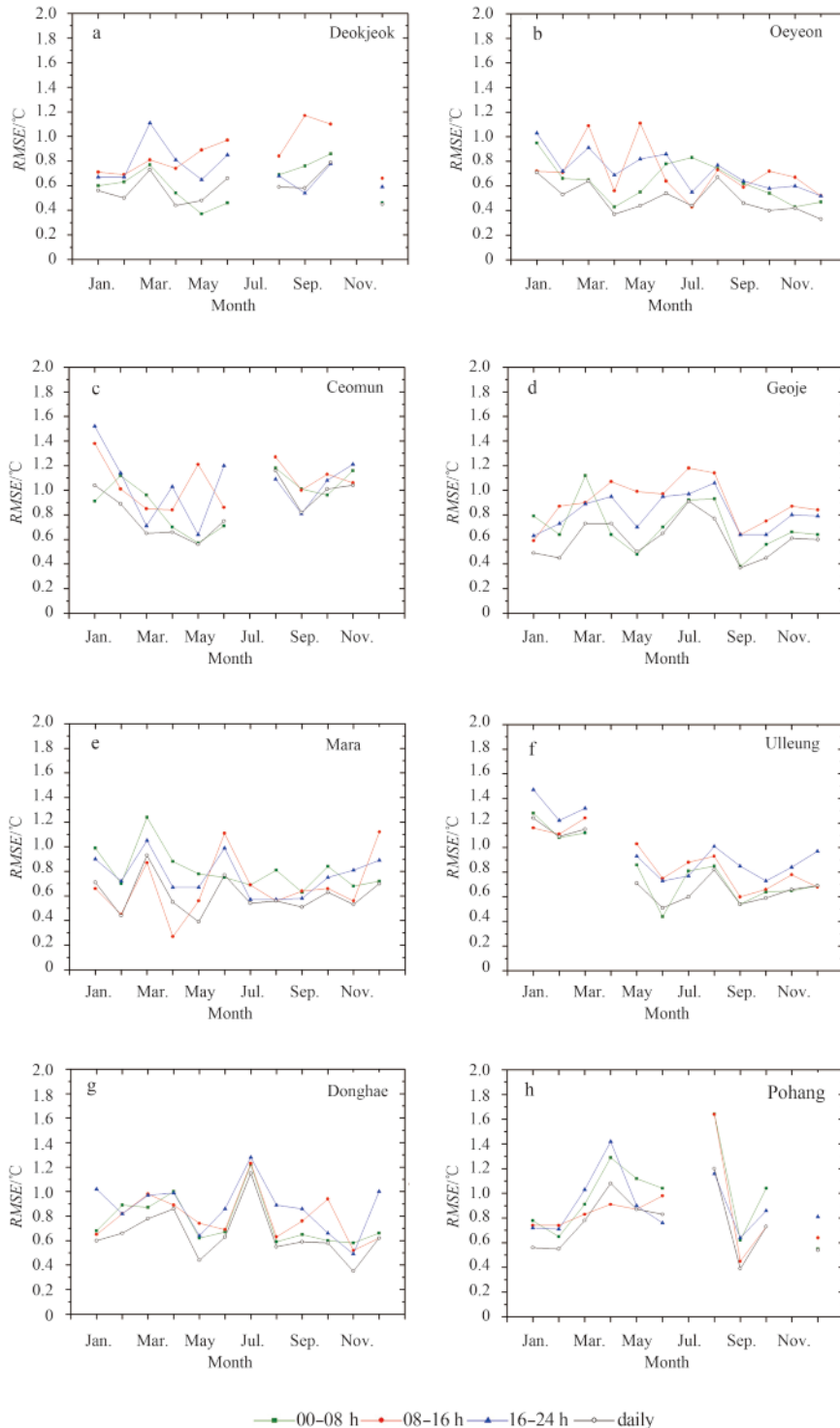**Fig. 12.** Scatter diagrams for comparison between the KIOST and the *in-situ* SSTs from eight locations.

Table 5. Statistics and accuracy of daily KIOST and *in-situ* SSTs (°C)

| Sites	Numbers of matched data	Mean±Std. of KIOST	Mean±Std. of *in-situ*	RMSE	(KIOST SST)–(*in-situ* SST)
Deokjeok	255	10.26 ±8.28	10.23 ±8.24	0.60	0.03
Geomun	254	16.91 ±5.44	16.57 ±5.31	0.83	0.34
Geoje	364	18.29 ±4.98	18.24 ±4.83	0.62	0.05
Donghae	364	17.44 ±5.34	17.55 ±5.14	0.75	−0.11
Pohang	302	17.11 ±5.29	17.22 ±5.09	0.83	−0.12
Mara	339	20.00 ±5.37	20.30 ±5.24	0.63	−0.29
Oeyeon	348	14.42 ±8.38	14.60 ±8.40	0.50	−0.17
Ulleung	333	17.60 ±5.89	17.86 ±5.32	0.86	−0.26
total/mean	2 559	16.70 ±6.73	16.79 ±6.61	0.71	−0.08

summer (July and August) than in other seasons. Although SSTs during the 16–24 h period in the East Sea/Sea of Japan sites (Donghae and Pohang) show highest RMSE values, the others have high values in the 08–16 h and 16–24 h data. At main sites except the East Sea/Sea of Japan sites, the RMSE values of SSTs during 08–16 h period are increased during summer season than in other seasons. Although these inaccuracies during summer may be caused by diurnal effects, it is necessary to analyze the data in detail with respect to the solar irradiance and rainfall dur-

ing summer season.

For objective validation, the independent *in-situ* data at the Ieodo site were used, which were not used in OI algorithm during 2013. Although the data were obtained at only one site, the accuracy of KIOST SST data was similar as in Fig. 13. As to the temporal RMSE variations, the RMSE values in May are highest during one year and the SST error during 08–16 h period is much greater than the other products.

Fig. 13. Temporal variations of the RMSE of one-month average KIOST SSTs from *in-situ* SSTs from January to December 2013.
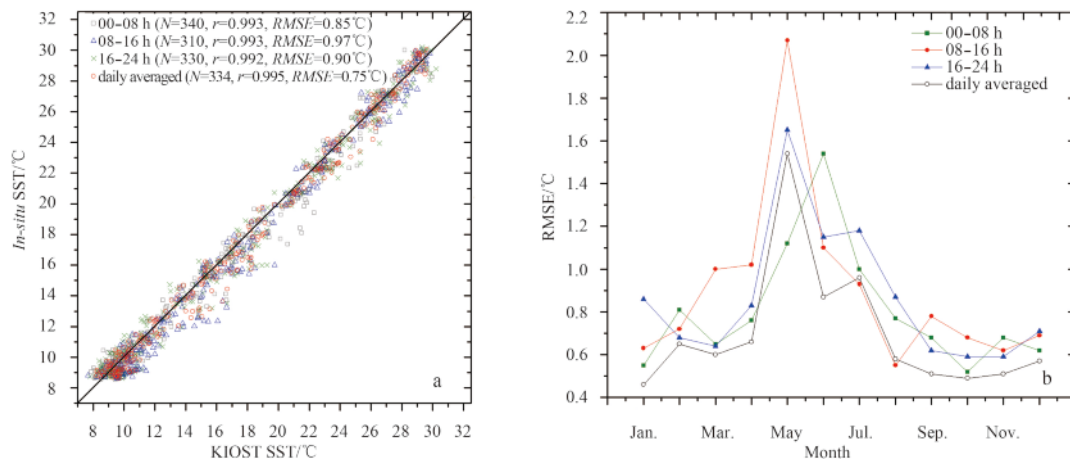
Fig. 14. Scatter diagrams for comparison between the KIOST and the *in-situ* SSTs (a), temporal variations of the difference of one-month average KIOST SSTs from *in-situ* SSTs at the Ieodo site from January to December 2013 (b).

5 Conclusions

The KIOST SST product generated by merging the *in-situ* temperature data and four IR and two microwave satellite SSTs is described. The infrared SST data include those acquired by the AVHRR, MODIS, MTSAT-2, and MI, and the microwave radiometer SSTs are those acquired by AMSR2 and WindSAT. The merging of these data is achieved by using the optimal interpolation (OI) algorithm. The product provides the mean SSTs at every 8 h on a daily basis with higher spatial resolution of 1 km in finer spatial structure than the GHRSST product. Using the data acquired from January to December 2013, it was shown that the daily KIOST SST product has the RMSE of 0.71°C and bias of –0.08°C as compared with the *in-situ* data. The SSTs in the Sea of Japan/East Sea and Southern Sea showed large spatial variations common to both the KIOST and GHRSST products. Among three 8 hourly SSTs, the 00–08 h SST data had the highest accuracy as compared with the *in-situ* data, followed by the 16–24 h and 08–16 h data. It should be emphasized that the KIOST SST products are very accurate showing the mean correlation coefficients over 0.99 with the *in-situ* SST data. During summer, the accuracy of 08–16 h data showed lower accuracy than the other products. The reason may be caused by diurnal effects, but further detailed analyses are required by taking into account the solar irradiance and rainfall during summer season. The work is currently in progress.

References

Bretherton F P, Davis R E, Fandry C B. 1976. A technique for objective analysis and design of oceanographic experiments applied to MODE-73. Deep Sea Research and Oceanographic Abstracts, 23(7): 559–582

Chao Yi, Li Zhijin, Farrara J D, et al. 2009. Blending sea surface temperatures from multiple satellites and in situ observations for coastal oceans. Journal of Atmospheric and Oceanic Technology, 26(7): 1415–1426

Donlon C J, Martin M, Stark J, et al. 2012. The operational sea surface temperature and Sea ice analysis (OSTIA) system. Remote Sensing of Environment, 116: 140–158

Donlon C J, Nykjaer L, Gentemann C. 2004. Using sea surface tem-

perature measurements from microwave and infrared satellite measurements. International Journal of Remote Sensing, 25(7–8): 1331–1336

Donlon C J, Robinson I, Casey K S, et al. 2007. The global ocean data assimilation experiment high-resolution sea surface temperature pilot project. Bulletin of the American Meteorological Society, 88(8): 1197

Goodrum G, Kidwell K B, Winston W. 2000. NOAA KLM User's Guide-September 2000 Revision. NOAA/NESDIS/NCDC

Guan Lei, Kawamura H. 2003. SST availabilities of satellite infrared and microwave measurements. Journal of Oceanography, 59(2): 201–209

Guan Lei, Kawamura H. 2004. Merging satellite infrared and microwave SSTs: Methodology and evaluation of the new SST. Journal of Oceanography, 60(5): 905–912

He Ruoying, Weisberg R H, Zhang Haiying, et al. 2003. A cloud-free, satellite-derived, sea surface temperature analysis for the West Florida Shelf. Geophysical Research Letters, 30(15): 1811

Kawai Y, Kawamura H, Takahashi S, et al. 2006. Satellite-based high-resolution global optimum interpolation sea surface temperature data. Journal of Geophysical Research, 111(C6): C06016, doi:10.1029/2005JC003313

Lee D-K, Niiler P P. 2005. The energetic surface circulation patterns of the Japan/East Sea. Deep-Sea Research Part II: Topical Studies in Oceanography, 52(11–13): 1547–1563

Lee D-Y, Park G-S, Shi Jun. 2009. Establishment of an Operational Oceanographic System for regional seas around Korea. Ocean and Polar Research, 31(4): 361–368

Legeckis R, Zhu Tong. 1997. Sea surface temperatures from the GOES-8 geostationary satellite. Bulletin of American Meteorological Society, 78(9): 1971–1983

Lie H-J, Cho C-H, Lee J-H, et al. 1998. Separation of the Kuroshio water and its penetration onto the continental shelf west of Kyushu. J Geophy Res, 103(C2): 2963–2976

Martin M, Dash P, Ignatov A, et al. 2012. Group for High Resolution Sea Surface Temperature (GHRSST) analysis fields inter-comparisons. Part 1: A GHRSST multi-product ensemble (GMPE). Deep-Sea Research Part II: Topical Studies in Oceanography, 77–80: 21–30

May D A, Parmeter M M, Olszewski D S, et al. 1998. Operational processing of satellite sea surface temperature retrievals at the Naval Oceanographic Office. Bulletin of American Meteorological Society, 79(3): 397–407

National Institute of Meteorological Research (NIMR). 2013. Research for the Meteorological and Earthquake Observation Technology and its Application [NIMR 2012-B-3](II). 180

Park M-H, Lee J-S, Ahn J-S, et al. 2014. A study on the effect of cold

water mass on observed air temperature in Busan. Journal of the Korean Association of Geographic Information Studies, 17(3): 132–146

Reynolds R W. 1988. A real-time global sea surface temperature analysis. Journal of Climate, 1(1): 75–87

Reynolds R W, Smith T M. 1994. Improved global sea surface temperature analyses using optimum interpolation. Journal of Climate, 7(6): 929–948

Reynolds R W, Zhang Huaimin, Smith T M, et al. 2005. Impacts of in situ and additional satellite data on the accuracy of a sea-surface temperature analysis for climate. International Journal of Climatology, 25(7): 857–864

Sakaida F, Kawamura H, Takahashi S, et al. 2009. Research and devel-

opment of the New Generation Sea Surface Temperature for Open Ccean (NGSST-O) product and its demonstration operation. Journal of Oceanography, 65(6): 859–870

Tanahashi S, Kawamura H, Matsuura T, et al. 2000. Improved estimates of wide-ranging sea surface temperature from GMS S-VIS-SR data. Journal of Oceanography, 56(3): 345–358

Wick G A, Bates J J, Scott D J. 2002. Satellite and skin-layer effects on the accuracy of sea surface temperature measurements from the GOES satellites. Journal of Atmospheric and Oceanic Technology, 19(11): 1834–1848

Wu Xiangqian, Menzel W P, Wade G S. 1999. Estimation of sea surface temperature using GOES-8/9 radiance measurement. Bulletin of American Meteorological Society, 80(6): 1127–1138